Robotica (2011) volume 29, pp. 1005–1015. © Cambridge University Press 2011
doi:10.1017/S0263574711000282

# Motion prediction and supervisory control of the macro–micro parallel manipulator system

Xuechao Duan, Yuanying Qiu, Jianwei Mi and Ze Zhao

*Research Institute on Mechatronics, School of Electromechanical Engineering, Xidian University, Xi'an 710071, P. R. China*

(Received in Final Form: March 10, 2011. First published online: April 11, 2011)

**SUMMARY**

This paper deals with the motion prediction and control of the macro–micro parallel manipulator system for a 500-m-aperture spherical radio telescope (FAST). Firstly, based on principles of parallel mechanism, a decoupled tracking and prediction algorithm to predict the position and orientation of the movable macro parallel manipulator is presented in this paper. Then, taken as the upper layer supervisory controller in the joint space of the micro parallel manipulator, the adaptive interaction PID controller utilizing the adaptive interaction algorithm to adjust the parameters of a canonical PID controller is discussed. In addition, the digital servo filters with feedforward are employed in the linear actuators as the lower layer controllers. Experimental results of a one-tenth scale FAST field model validate the effectiveness of the supervisory controller and the motion prediction algorithm.

KEYWORDS: Macro–micro parallel manipulator; Supervisory control; Tracking and prediction; Adaptive interaction; Forward position kinematics; Stewart platform.

## 1. Introduction

As one of the national major scientific infrastructures in China, the 500-m-aperture spherical radio telescope (FAST) is being built in the unique karst limestone depressions in the southwest of China.[1] FAST will be the largest single dish reflector radio telescope. Consequently, it is hoped to reveal the dawn of galaxy formation, as well as many other new discoveries in all fields of astronomy. As a matter of fact, constructing such a FAST is a challenging task, but this is not the first attempt because a similar one exists: the Arecibo observatory in Puerto Rico, with a diameter of 305 m.[2,3] From the viewpoint of engineering-oriented techniques, FAST is not a simple copy of the Arecibo telescope but has a number of innovations. The two prominent distinctions are as follows. First, the active main spherical reflector, obtained by deforming the illuminated area to a paraboloid of revolution in real time, enables the realization of both wide bandwidth and full polarization capability, while using a conventional feed design. Second, the macro–micro parallel manipulator system for feed source supporting, pointing, and orientating – which integrates optical, mechanical, and electronic technologies – effectively reduces the cost of the supporting structure,[4,5] as shown in Fig. 1.

* Corresponding author. E-mail: xchduan@xidian.edu.cn

The six cables driven by servo motors and winches are the limbs of the macro parallel manipulator, and the cabin is its end-effector. The feed source (radio waves receiver) of FAST is required to move along the preset trajectory with a root-mean-square (RMS) error of 4 mm. As the precision of the six-cable-driven parallel manipulator can not satisfy the astronomical specification due to the flexibility of cables, a rigid Stewart platform acting as the micro parallel manipulator is mounted on the bottom of the cabin, and the feed source is mounted on the mobile platform (feed platform) of the Stewart platform to guarantee the high precision of the feed source. A rigid (micro) robot mounted serially to the tip of a flexible (macro) robot is often used to increase reachable workspace, but flexibility in the macro manipulator can make it susceptible to vibration.[6,7] Therefore, when the dexterous Stewart platform is mounted on the flexible cabin, it loses its accuracy and speed due to the compliance of the cabin. In literature, such a system is known under the name of underactuated system as well. This system is characterized by the number of control actuators being less than the number of state variables.[8,9]

The kinematics, dynamics, and motion control of a rigid Stewart platform have been studied extensively in the case when the base is fixed on the ground.[10,11] However, cases involving a large-span cable-driven parallel manipulator are rarely investigated. Studies regarding macro–micro manipulator systems have been conducted for many years,[12] such as modeling and control of macro–micro manipulators. Magee and Book[13] used command filtering to prevent the excitation of macro flexible modes, but their work focused on the joint controller. Lew and Trudnowski[14] adopted the inertial forces of the high-bandwidth micro manipulator to dampen the vibration of the macro manipulator. Yim and Sahjendra[15] used an inverse control law combined with a predictive control law for a macro–micro manipulator. Sharf[16] employed a two-stage controller determining the trajectory of the micro links to dampen the vibrations of the macro manipulator and, subsequently, to bring the micro part to a rest. Cheng and Patel[17] used a stable feedforward neural network to identify the macro–micro manipulator dynamics online and two inverse dynamics controllers for tracking and vibration suppression. Bassan *et al.*[18] studied macro–micro manipulators consisting of a rigid micro manipulator mounted on a flexible macro manipulator. They developed a control strategy consisting of a rigid body inverse dynamics controller together with a neural network-based strategy in order to dampen the oscillations caused by the

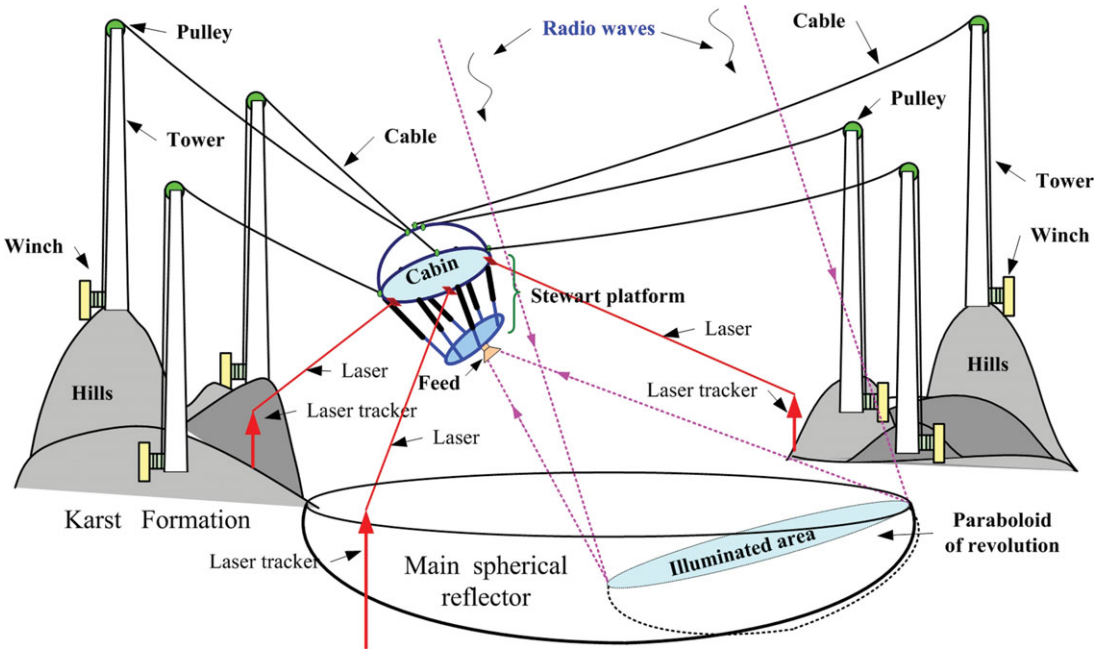


Fig. 1. Macro–micro parallel manipulator system for FAST.

flexible base. Mannani and Talebi[19] proposed a class of model-free fuzzy controllers based on the Lyapunov-function reasoning for a macro–micro manipulator system.

However, most macro–micro system consists of two serially combined rigid serial manipulators. Such a macro–micro manipulator system in this research is seldom studied. Consequently, the control strategy of the micro manipulator considering the vibrations of the macro manipulator is of great significance. The vibration of the cabin is caused by external wind disturbance and the internal dynamical compliance of the Stewart platform and internal nonlinearity. The essential issue is how to achieve the positioning and orientating precision of the feed platform by making use of the micro parallel manipulator.

This paper is organized as follows. The macro–micro parallel manipulator system configuration for FAST is introduced in Section 2, with an emphasis on the control model. The measuring and motion predictions of the cabin are presented in Section 3. Section 4 discusses real-time forward position kinematics, a key component for three-dimensional motion prediction. The controller design of the Stewart platform is explored in Section 5, and experimental results are given in Section 6. Finally, a few meaningful conclusions are drawn in Section 7.

## 2. System Descriptions

The FAST 50 m feed supporting and tracking system model is constructed according to a one-tenth proportion of the FAST prototype. It is expected to verify the mechanical model and software and to validate the control and measurement strategy. Further, researchers hope to draw rational conclusions regarding the FAST prototype from the FAST 50 m model.

The macro parallel manipulator for coarse tuning is driven by six large span steel cable servo systems, with the semi-spherical cabin as the end-effector. The cabin has a diameter of 1.0 m and a mass of 120.0 kg. Its center of gravity lies at the point located 4.9 cm vertically from the center of the bottom. Inside the cabin, there is a steel beam structure to enhance the stiffness and to save space to hold the drive units of the micro parallel manipulator. The semi-spherical steel mask of the cabin can decrease the wind load. The extendable driving system is comprised of an AC servomotor and drive unit, cycloidal reducer (reduction ratio: 1:60), and bobbin. The bobbin has a diameter of 0.4 m and can carry 20 turns of the cable. The servomotor and driver used in this model are the PANASONIC MHMA 502 AC servomotor, with an incremental encoder (2500 P/Rev) and the matching MHDA 503 driver, respectively. The motor parameters are as follows: rated power 5 kW, rated torque 23.8 N m, and rated speed 2000 rpm. The servo drive operates in the position mode and receives modulated pulses from a pulse distribution card developed by the authors. The card is embedded in the EISA socket of the micro tuning computer. The number of pulses indicates the motion value, and the frequency indicates the speed of each motor. The six-cable towers symmetrically standing on the same circle with a diameter of 50 m have the same height of 21 m. The multistranded steel cable has a radius of 0.521 cm and a linear density of 0.14 kg/m. The ends of the six cables are connected to the feed cabin with spherical joints. Finally, the location of the joints has been optimized in order to meet the requirement of the orientation of 60°.[20]

The micro parallel manipulator is a Stewart platform, which employs six identical precision linear actuators as driving limbs, each of which is connected to the cabin through a universal joint and connected to the platform (mobile platform) through a spherical joint. The feed platform is considered to be the end-effector of the micro manipulator. The linear actuators used in the research are THOMSON TN-series TN-BK23-10-5A-10 with an incremental encoder

https://doi.org/10.1017/S0263574711000282 Published online by Cambridge University Press

(8192 P/5 mm). The linear actuator has a basic length of 146.1 mm and a stroke length of 254 mm. The main parameters are as follows: maximum velocity 305 mm/s, maximum acceleration 7.7 m/s$^2$, maximum thrust 2670 N, total mass 5.5 kg, and repeatability +/−0.013 mm. The six drive units for the linear actuators are connected one by one with an RJ-45 cable and then connected to the MEI network motion controller, which is inserted in the PCI socket of the micro tuning computer. The MEI XMP-SynqNet-PCI motion controller is adopted here so that the up to 100 m remote control of the Stewart platform can be realized. The parameters of the motion controller are as follows: DSP Analog Devices SHARC 32-bit floating point, speed 40 MHz, update rate user programmable, velocity, acceleration, and jerk 32-bit floating point. The Stewart platform has a gross mass of 37.3 kg. The six universal joints divided into three pairs are symmetrically distributed on a circle with a diameter of 720 mm. The central angle for each pair of joints is 87°. The feed platform has a diameter of 280 mm on which the spherical joints have a similar distribution with the 31° central angle. The task space of the Stewart platform is a sphere with a radius of 75 mm. The initial height of the feed platform – i.e., the center of the task space – is −630 mm in the cabin frame.

In view of the large workspace of the cabin, an API (Automated Precision Instrument Inc.) Tracker 3–15 laser tracker sensor is used to accomplish the noncontact laser measurement. The main specifications are as follows: range of measurements 30 m in diameter; angular range azimuth: ±320°; elevation: +77°/−60°; angular resolution: ±0.018 arc s; angular accuracy: 3.5 $\mu$m/m; and maximum lateral target speed: >3 m/s (120°/s). With the six-degree-of-freedom target mounted on the cabin and the measurement program written by the authors, the real-time position and orientation of the cabin are obtained. The measuring data are updated at a frequency of 330 Hz and are transferred via the LAN.

As shown in Fig. 2, there are four EVOC industrial computers with Pentium IV-2.4 GHz in total in the field model. The computers are connected to a LAN to communicate with each other and to achieve the measuring and control goals. The task distribution of the four computers is as follows. The measuring computer deals with the real-time measuring data and sends them to the main control computer. The main control computer generates the motion trajectory of the macro–micro parallel manipulator system and then sends the trajectory data to the macro tuning computer. The macro tuning computer conducts the kinematic computation and feedback control of the macro parallel manipulator with the pulse distribution card. The micro tuning computer carries out the decoupled position and orientation prediction, adaptive interaction PID (AIPID) supervisory control, and kinematic computation of the Stewart platform, and then, it sends the control values of the six linear actuators to the SynqNet-PCI motion controller. The precise execution level servo control of the linear actuators is accomplished by the SynqNet-PCI motion controller. Each computer has a graphical user interface, which is used to display the status of the measuring and control process and to input control commands and parameters.

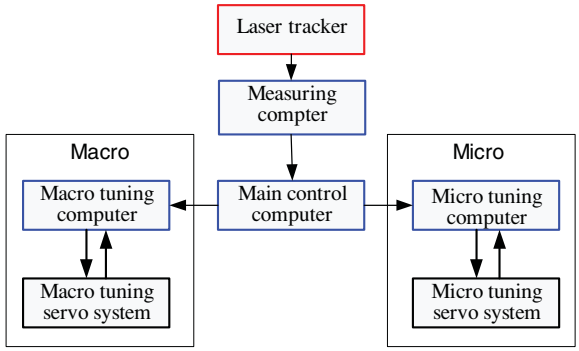


Fig. 2. Information flow of the measurement and control.

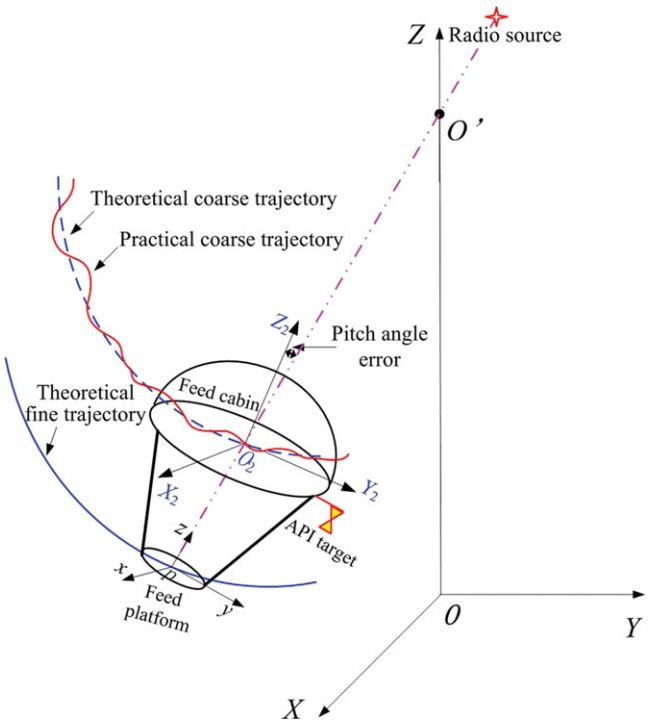


Fig. 3. Trajectory of the macro–micro parallel manipulator system.

The trajectory generation of the feed platform is the precondition for the successful astronomical observation of FAST, as shown in Fig. 3. The trajectory generation strategy for the macro–micro manipulator can be described as follows. The theoretical trajectory of the platform (fine trajectory) is determined by the desired trajectory of the radio telescope. In order to achieve the best receiving effect of the radio wave, the $z$-axis of the feed platform must point to the radio source to be observed all the time. Then, the theoretical trajectory of the cabin (coarse trajectory) can be determined according to the initial configuration of the Stewart platform. However, in the control process, the desired orientation of the platform depends on the real-time position and orientation of the cabin.

The frame $OXYZ$ in Fig. 3 is taken as the global frame. The mobile frame $O_2X_2Y_2Z_2$ fixed on the cabin is used to describe the position and orientation of the cabin. The frame $pxyz$ fixed on the feed platform describes the position and orientation of the platform. The position of the feed source at time $t$ is determined by the astronomical law of the radio

https://doi.org/10.1017/S0263574711000282 Published online by Cambridge University Press

source. The feed source is realized with circular polarization; therefore, the rotation of the feed source around its own symmetrical axis (local $z$-axis) does not impact the observing effect. For the observing purpose of FAST, only the pitch angle (the included angle between the $Z_2$- and $Z$-axes) of the platform is of great importance. However, for robotic control of the Stewart platform, the position and orientation of the platform must be specified uniquely. So, we choose the following equation:

$$^{w}z = \frac{\overline{OO'} - \overline{Op}}{\|\overline{OO'} - \overline{Op}\|}, \tag{1}$$

where $^{w}z$ is the unit vector of the $z$-axis in the global frame. Equation (1) makes the feed source point to the radio object. The following Eq. (2) makes the Stewart platform tend to keep the initial configuration so that the parallel manipulator has high stiffness, precision, and servo bandwidth.[21,22]

$$\begin{cases} ^{w}x = \overline{O_2Y_2} \times \overline{O_2Z_2} \\ ^{w}y = ^{w}z \times ^{w}x. \end{cases} \tag{2}$$

The supervisory controller is often used in the control of an underactuated system, such as the positioning control of a manipulator mounted on an oscillatory base. The main function of the supervisory controller is to use available data to characterize the overall system's current behavior, potentially modifying the lower level controllers to ultimately achieve the desired specification. Additionally, the supervisor may be employed to integrate other information into the control decision-making process. Given this information, the supervisor can tune the supervised controller for better performance. Consequently, in the control of a macro–micro manipulator system, a supervisory controller is needed to generate the planning level control value of the Stewart platform according to the actual position and orientation of the cabin. With the fine-tuning motion of the Stewart platform, the impact of dynamical tracking error of the cabin on the feed platform can be eliminated.

## 3. Measuring and Prediction of the Cabin

The response of the cabin induced by external excitation is unknown. Thus, in the control process of the Stewart platform, in order to overcome the influence of the flexibility of the cabin and cable structure on the platform, it is desirable to set the control value of the platform at the current moment $t$ as the function of both the theoretical position and orientation of the platform and the actual position and orientation of the cabin, at the $t + \Delta t$ ($\Delta t$ denotes the control period) moment. The theoretical position and orientation of the platform have mathematical expressions. The actual position and orientation of the cabin at $t + \Delta t$ is the dynamical response for the stochastic external disturbance and the dynamical compliance between the cabin and Stewart platform. From the engineering point of view, the prediction of the future position and orientation of the cabin based on the current and previous measuring data is a feasible solution. Therefore, the control value is obtained by the following equations:

$$\begin{cases} \boldsymbol{l}_{\mathrm{ab}}(t + \Delta t) = G(^{\mathrm{G}}\boldsymbol{X}_{\mathrm{PT}}(t + \Delta t), ^{\mathrm{G}}\tilde{\boldsymbol{X}}_{\mathrm{BR}}(t + \Delta t)), \\ \Delta \boldsymbol{l}_{\mathrm{ab}} = f_{\mathrm{sc}}(\boldsymbol{l}_{\mathrm{ab}}(t + \Delta t) - \boldsymbol{l}_{\mathrm{ab}}(t)), \end{cases} \tag{3}$$

where $\boldsymbol{l}_{\mathrm{ab}}(t)$ is the six-dimensional vector consisting of the length of the six legs, and $G(\cdot)$ represents the inverse kinematic function of the Stewart platform. $^{\mathrm{G}}\boldsymbol{X}_{\mathrm{PT}}(t + \Delta t)$ denotes the position and orientation of the cabin at the moment of $t + \Delta t$, and $f_{\mathrm{sc}}(\cdot)$ represents the function of the supervisory controller. $^{\mathrm{G}}\tilde{\boldsymbol{X}}_{\mathrm{BR}}(t + \Delta t)$ represents the predicted value of the position and orientation of the cabin at the moment of $t + \Delta t$, which is predicted according to the following algorithm.

As a three-dimensional maneuvering object, the cabin has six degrees of freedom. Here $X$, $Y$, and $Z$ are used to describe the position of the reference point, while the roll, pitch, and yaw angle set consisting of $\phi, \theta$, and $\psi$ is used to describe the orientation of the cabin. The conventional position and orientation prediction algorithm for a three-dimensional maneuvering object is as follows:

(1) In each degree of freedom, the linear or angular velocity is obtained from the measured position and orientation data by using the numerical differential operation;
(2) According to the large inertia of the cabin, its movement in each degree of freedom is assumed to be a uniformly accelerated linear motion in each duration $\Delta t$. Therefore, the position and orientation of the cabin can be predicted with the equation of the uniformly accelerated linear motion.

However, there exist two shortcomings in this prediction scheme:

(1) The motion of the cabin is decomposed into six degrees of freedom artificially. As a result, the coupling property of the cabin is broken;
(2) The measured data are quite noisy, and the conventional numerical differential operation often amplifies the noise signals. Moreover, a lesser value for $\Delta t$ leads to a more significant amplification effect.

In order to overcome the first shortcoming mentioned above, a new tracking and prediction algorithm based on the theory of parallel mechanism is presented. In this algorithm, the cabin is treated as the end-effector of a suppositional, six degree-of-freedom, fully parallel manipulator. The configuration parameters of the suppositional parallel manipulator have been optimized so that it has well-conditioned kinematic transmissivity. The suppositional end-effector – i.e., the cabin – is measured with a noncontact laser measurement, so at any moment $t$, the inverse kinematics of the suppositional parallel manipulator can be conducted. Therefore, the six suppositional leg lengths can be determined. The parallel manipulator has a decoupled joint space, so leg lengths are predicted in the joint space. The leg lengths of the parallel manipulator in next moment can be described as

$$\tilde{L}_i(t + \Delta t) = L_i(t) + v_{\mathrm{l}_i}(t)\Delta t + 0.5a_{\mathrm{l}_i}(t)\Delta t^2, \tag{4}$$

https://doi.org/10.1017/S0263574711000282 Published online by Cambridge University Press

where $i = 1, 2, \ldots, 6$, $\tilde{L}_i$ is the predicted value of the $i$th leg of the suppositional parallel manipulator, $v_{l_i}(t)$ is the length adjustable speed of the $i$th leg, and $a_{l_i}(t)$ is the length adjustable acceleration of the $i$th leg. Ultimately, the future position and orientation ${}^{\mathrm{G}}\tilde{\boldsymbol{X}}_{\mathrm{BR}}$ of the cabin are obtained with the forward position kinematics of the suppositional parallel manipulator.

From the kinematics point of view, there exists a linear relation among the position, velocity, and acceleration of a moving object. In the conventional prediction algorithm, the numerical difference operation is employed to obtain the velocity signal from the position signal and the acceleration signal from the velocity signal. However, the canonical numerical differential operation amplifies the noise signal. In general, a low-pass filter should be utilized together with the numerical difference for improvement. Simultaneously with high-frequency noise signal suppression, the phase delay will be introduced. The servo bandwidth of the system would be narrowed; moreover, the stability of the system may be destroyed. Hence, a nonlinear tracking differentiator with a high-quality differential signal abstraction function is used in this research in order to obtain the velocity and acceleration of the legs from the leg length data.

The tracking differentiator is one of the key parts of active disturbance rejection controller proposed by Han.[12,23,24] It achieves the goals of obtaining the differential signals from discontinuous or noisy measuring signals in engineering practice. This prediction algorithm must abstract the velocity and acceleration signals from the leg length signals.

The second-order typical tracking differentiator has the following discrete form:

$$\begin{cases} r_1(k+1) = r_1(k) + h \cdot r_2(k), \\ r_2(k+1) = r_2(k) + h \cdot fhan(r_1(k) - r(k), r_2(k), \delta, h). \end{cases} \tag{5}$$

where $h$ is the sampling step and $\delta$ is the velocity factor that determines the transient process. The nonlinear function $fhan(x_1, x_2, \delta, h)$ is expressed by

$$fhan(x_1, x_2, \delta, h) = \begin{cases} -\delta \cdot \mathrm{sgn}(a), & |a| > d, \\ -\delta \cdot a/d, & |a| \le d, \end{cases} \tag{6}$$

where $\mathrm{sgn}(\cdot)$ denotes the sign function. The parameters $a$ and $d$ of the nonlinear function are defined as the following:

$$a = \begin{cases} x_2 + \dfrac{a_0 - d}{2}\mathrm{sgn}(y), & |y| > d_0, \\ x_2 + y/2, & |y| \le d_0, \end{cases} \tag{7}$$

$$\begin{cases} d = h\delta, d_0 = hd, \\ y = x_1 + hx_2, \\ a_0 = \sqrt{d^2 + 8\delta\,|y|}, \end{cases} \tag{8}$$

where $d$ and $d_0$ are switching thresholds of the function, $y$ is the combinatorial value of the state variables, and $a$ and $a_0$ are the net increments of the state variable values of the function.

For any limitary integrable function $r(t)$, the two signals $r_1(t)$ and $r_2(t)$ provided by Eq. (5) can track $r(t)$ and $\dot{r}(t)$, respectively, i.e., $\lim_{t\to\infty}[r(t) - r_1(t)] = 0$, $\lim_{t\to\infty}[\dot{r}(t) - r_2(t)] = 0$. For the parameter $\delta = 25,000$, the initial condition is set as $r_1(0) = 0$, $r_2(0) = 0$. In this algorithm, the second-order differential signal of the leg length signal is required; consequently, two tracking differentiators are used serially to achieve the goal.

## 4. Real-Time Forward Position Kinematics

Many researchers have studied the forward position kinematics of the parallel manipulator.[25] Aiming at the online implementation, a real-time algorithm for forward position kinematics of the fully parallel manipulators is proposed, in which the steepest descent direction of the solution iteration is constructed with a Jacobian matrix, with an initial position for iteration arbitrarily chosen from the workspace. Under the conditions of motion continuity of the end-effector, the unique forward position kinematics solution can be determined with this algorithm.

The Cartesian workspace of the parallel manipulator is assumed to be singular-free. This is the case in practical applications. For a moving process of the end-effector, $\boldsymbol{P}^0$ is the hypothetical initial point from which the parallel manipulator starts this movement and reaches the unknown present point $\boldsymbol{P}^d$. The leg length vector is represented by $\boldsymbol{L}^d$, each component of which can be calculated by the feedback reading of the driving mechanism – for instance, revolute or linear optical encoders. In addition, $\boldsymbol{P}^0$ can be an arbitrary point within the workspace. The role of forward position kinematics here is to find the specified value of $\boldsymbol{P}^d$ by taking advantage of $\boldsymbol{P}^0$ and $\boldsymbol{L}^d$. For this purpose, the following iteration algorithm on the basis of steepest descent principle is developed:

Step 1: Given the initial position $\boldsymbol{P}^0$ and leg length vector $\boldsymbol{L}^d$, let $\varepsilon > 0$ be the convergence accuracy of the algorithm and $k = 0$.

Step 2: The leg length vector of the parallel manipulator at the present position and orientation should be solved by the inverse position kinematics, i.e., $\boldsymbol{L}^k = InvKin(\boldsymbol{P}^k)$. The error vector of leg length between $\boldsymbol{L}^d$ and $\boldsymbol{L}^k$ – namely, $\Delta\boldsymbol{L}^k = \boldsymbol{L}^d - \boldsymbol{L}^k$ – is calculated.

Step 3: Calculate the negative increment of position and orientation $\boldsymbol{S}^k = -\boldsymbol{J}^{-1}(\boldsymbol{P}^k)\Delta\boldsymbol{L}^k$. If $\|\boldsymbol{S}^k\| \le \varepsilon$, the algorithm will stop and $\boldsymbol{P}^d = \boldsymbol{P}^k$; otherwise, continue to Step 4.

Step 4: Obtain the new position and orientation $\boldsymbol{P}^{k+1} = \boldsymbol{P}^k + \boldsymbol{S}^k$, and let $k = k + 1$, so go to Step 2.

**Theorem** (**Convergence theorem**). The algorithm aforementioned will converge to $\boldsymbol{P}^d$ after finite iterations, and inverse position kinematics of the resulting point is $\boldsymbol{L}^d$.

**Proof.** The motions of a parallel manipulator between joint space and task space are mapped nonlinearly. The inverse kinematics model is used to change the position or the velocity of the end-effector into the lengths and velocities of the parallel limbs or legs. This is the base for the control of parallel manipulators due to the fact that the control instructions of driving components, motors, or hydraulic actuators must be obtained from their lengths at different times. The nonlinear mapping relationship between the end-effector and the leg lengths of a parallel manipulator can

https://doi.org/10.1017/S0263574711000282 Published online by Cambridge University Press

generally be denoted as follows:

$$\boldsymbol{L} = InvKin(\boldsymbol{P}), \tag{9}$$

where the vector $\boldsymbol{P}$ indicates the position and orientation of the end-effector with six degrees of freedom, and $\boldsymbol{L} = [L_1, L_2, \ldots, L_6]^{\mathrm{T}}$ is the leg length vector. The velocity transformation from the task space to joint space is linear by a celebrated matrix called the Jacobian. That is to say,

$$\dot{\boldsymbol{L}} = \boldsymbol{J}\dot{\boldsymbol{P}}, \tag{10}$$

where $\dot{\boldsymbol{P}}$ is indicative of the $N$-degree-of-freedom general velocity, $\dot{\boldsymbol{L}} = [\dot{L}_1, \dot{L}_2, \ldots, \dot{L}_6]^{\mathrm{T}}$ is the sliding velocity vector of legs, and $\dot{L}_i$ $(i = 1, 2, \ldots, 6)$ is the sliding velocity of the $i$th leg. Equation (10) can be rewritten as

$$\frac{\mathrm{d}\boldsymbol{L}}{\mathrm{d}t} = \boldsymbol{J}\frac{\mathrm{d}\boldsymbol{P}}{\mathrm{d}t}.$$

By the definition of the differential, we have

$$\Delta\boldsymbol{L} = \boldsymbol{J}\Delta\boldsymbol{P}, \tag{11}$$

where $\Delta\boldsymbol{L}$ and $\Delta\boldsymbol{P}$ are the differentials of the leg length vector $L$ and $P$, respectively. As it is assumed that no singularity in the workspace of the parallel manipulator has been established, no singular phenomenon will occur in our discussion. In the view of the Jacobian, that is to say,

$$|\boldsymbol{J}| \neq 0.$$

Corresponding to Eq. (11), the following relationship is obtained:

$$\Delta\boldsymbol{P} = \boldsymbol{J}^{-1}\Delta\boldsymbol{L}. \tag{12}$$

The scalar function of position and orientation error is defined as follows:

$$f(\boldsymbol{P}) = \tfrac{1}{2}\|\boldsymbol{P} - \boldsymbol{P}^d\|^2 = \tfrac{1}{2}(\boldsymbol{P} - \boldsymbol{P}^d)^{\mathrm{T}}(\boldsymbol{P} - \boldsymbol{P}^d). \tag{13}$$

The gradient of $f(\boldsymbol{P})$ at point $P$ is

$$\nabla f(\boldsymbol{P}) = \frac{\partial f}{\partial \boldsymbol{P}} = \boldsymbol{P} - \boldsymbol{P}^d = \boldsymbol{J}^{-1}(\boldsymbol{P})\Delta\boldsymbol{L}.$$

Therefore, $\boldsymbol{S} = -\boldsymbol{J}^{-1}(\boldsymbol{P})\Delta\boldsymbol{L}$ in Step 3 of the algorithm is in fact the steepest descent direction, i.e., negative gradient direction, of $f(\boldsymbol{P})$. According to the nonrestraint optimization theories,[26] a vector series of $\{\boldsymbol{P}^k\}$ generated by this algorithm should converge to the only stationary point, which is denoted as $\boldsymbol{P}^*$. Furthermore, $\Delta\boldsymbol{P}^k = \nabla f(\boldsymbol{P}^*) = 0$.

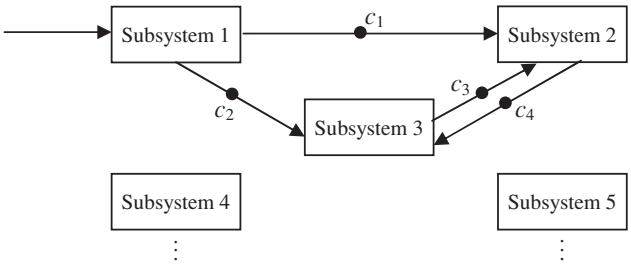


Fig. 4. Subsystems and interactions.

This is in addition to the following:

$$f(\boldsymbol{P}) = \tfrac{1}{2}\|\boldsymbol{P} - \boldsymbol{P}^d\|^2 \geq 0.$$

Considering the movement continuation and small range of the end-effector in the control process, $f(\boldsymbol{P})$ has exactly one minimum point $\boldsymbol{P}^d$ in the neighborhood of $\boldsymbol{P}^0$. Namely, $f(\boldsymbol{P}^*) = f(\boldsymbol{P})_{\min} = f(\boldsymbol{P}^d) = 0$ and $\boldsymbol{P}^* = \boldsymbol{P}^d$ hold, which illustrates that the steepest descent algorithm can achieve the desired position and orientation vector $\boldsymbol{P}^d$ associated with leg length vector $\boldsymbol{L}^d$. This is the end of the proof.

## 5. Controller Design

The adaptive interaction algorithm is based on the adaptive interaction theory proposed by Brand and Lin.[27,28] This algorithm has found applications in neural network learning and PID control parameter adjusting, as a result of its easy implementation and good robustness. The adaptive interaction theory divides a complicated system into $N$ subsystems. The input $x_i$ and output $y_i$ of each subsystem are both integrable. The dynamics performance of each subsystem can be expressed with a causal function, as follows:

$$y_i(t) = (F_i \circ x_i)(t) = F_i[x_i(t)], \quad i = 1, 2, \ldots, N, \tag{14}$$

where $\circ$ denotes the function composition.

It is assumed that the derivative of $F_i$ exists. Further, it is assumed that each subsystem is a single-input and single-output (SISO) system. The interaction between the two subsystems consists of a functional dependence of the input of one of the subsystems on the outputs of the others, and it is mediated by information-carrying connections denoted by $c_i$. The set of all connections is denoted by $C$. A typical system structure is shown in Fig. 4. $I_i$ and $O_i$ are defined as the input and output of the $i$th subsystem, respectively. For subsystem 2,

$$I_2 = \{c_1, c_3\}, \quad O_2 = \{c_4\}. \tag{15}$$

For the simplicity of analysis, we simplify the problem. It is assumed that only linear interactions exist among subsystems. Note that the input of the $i$th subsystem can be expressed by the linear combination of the outputs of other subsystems

$$x_i(t) = u_i(t) + \sum_{c \in I_i} \alpha_c y_{ic}(t), \tag{16}$$

https://doi.org/10.1017/S0263574711000282 Published online by Cambridge University Press

where $u_i(t)$ is the external input signal of the $i$th subsystem, $\alpha_c$ is the connection coefficient, and $y_{ic}(t)$ denotes the input signal of $c_i$ connecting to the $i$th subsystem.

According to the linear interaction function, the dynamic relation of the subsystems can be expressed by

$$y_i(t) = F_i\left[u_i(t) + \sum_{c\in I_i} \alpha_c y_{ic}(t)\right], \quad i = 1, 2, \ldots, N. \quad (17)$$

The purpose of the adaptive interaction algorithm is to minimize the given performance function $E(y_1, y_2, \ldots, y_N, u_1, u_2, \ldots, u_N)$ by adjusting the connection coefficients $\alpha_c$ among subsystems adaptively.

The proof given by Lin[28] shows that when the connection coefficients in Eq. (17) vary according to Eq. (18), then Eq. (19) is the only solution for Eq. (17), and the performance function $E$ decreases with time.

$$\dot{\alpha}_c = \left(\sum_{s\in O_{o_c}} \alpha_s \dot{\alpha}_s \frac{\frac{\mathrm{d}E}{\mathrm{d}y_{o_s}} \circ F'_{o_s}}{\frac{\mathrm{d}E}{\mathrm{d}y_{o_s}} \circ F'_{o_s} \circ y_{o_c}} - \gamma \frac{\partial E}{\partial y_{o_c}}\right) \circ F'_{o_c} \circ y_{o_c}, \quad (18)$$

$$\dot{\alpha}_c = -\gamma \frac{\mathrm{d}E}{\mathrm{d}\alpha_c}, \quad (19)$$

where $y_{o_c}$ denotes the output signal of $c$ connecting to the subsystem. $\boldsymbol{O}_{o_c}$ is the output connection set of $c$, the adaptive coefficient $\gamma$ is selected according to the specific characteristic, and $\gamma$ is often a positive real number.

The PID control algorithm has found wide applications in process control and servo control fields due to its simple structure, good robustness, and high reliability. As a matter of fact, the PID controller is linear. It controls the plant by incorporating the proportional, integral, and differential values of the error signal. A typical continuous PID control algorithm is expressed by

$$u(t) = K_P e(t) + K_I \int e(t)\,\mathrm{d}t + K_D \frac{\mathrm{d}e(t)}{\mathrm{d}t}, \quad (20)$$

where $u(t)$ is the control signal and $e(t)$ is the error signal. According to the adaptive interaction theory, a PID control system can be divided into four loops (or subsystem): the proportional loop, the integral loop, the differential loop, and the plant loop.

The adaptive connection coefficient is $\alpha_c = (K_P, K_I, K_D)$, and $O_4 = y_4$. The absolute error function of the system is defined as the performance index, i.e., $E = e^2 = (u - y_4)^2$. Then, Eq. (19) can be equivalent to the following:

$$\begin{cases} \dot{K}_P = 2\gamma e F'_4[x_4] \circ y_1, \\ \dot{K}_I = 2\gamma e F'_4[x_4] \circ y_2, \\ \dot{K}_D = 2\gamma e F'_4[x_4] \circ y_3. \end{cases} \quad (21)$$

It is shown that the adaptive adjustment algorithms for $K_P$, $K_I$, and $K_D$ have the same form.[28] They all depend on the error of the control system, the Frechet differential value of $F_4[x_4]$ and the output of the PID component $y_i$, $i = 1, 2, 3$. They are all independent of the substantial characteristic. In most contexts, $F'_4[x_4] \circ y_1$, $F'_4[x_4] \circ y_2$ and $F'_4[x_4] \circ y_3$ can be linearized as follows:

$$\dot{K}_P = 2\gamma e y_1, \quad \dot{K}_I = 2\gamma e y_2, \quad \dot{K}_D = 2\gamma e y_3. \quad (22)$$

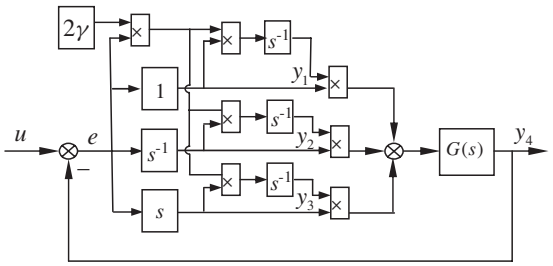


Fig. 5. AIPID control system.

Table I. Parameters of PID filters for the legs.

| No. | $k_p$ | $k_i$ | $k_d$ |
|---|---|---|---|
| 1 | 60.0 | 100.0 | 250.0 |
| 2 | 60.0 | 100.0 | 200.0 |
| 3 | 40.0 | 100.0 | 250.0 |
| 4 | 40.0 | 100.0 | 200.0 |
| 5 | 40.0 | 100.0 | 250.0 |
| 6 | 40.0 | 100.0 | 200.0 |

As shown in Fig. 5, a typical PID controller incorporated with the simplified adaptive interaction adjustment algorithm is an AIPID controller. If the AIPID controller is employed directly to control the plant $G(s)$, then the AIPID is an executive level controller (also called a compensator) and receives feedback from outside the control loop. In this research, the AIPID is a supervisory controller and does not directly receive feedback values from the legs of the Stewart platform. In addition, the supervisory controller deals with the motion planning signals in the upper level.

The AIPID controller is SISO, so it should be utilized in the decoupled joint space. The final AIPID supervisory control block is shown in Fig. 6. The block of AIPID denotes the six-channel AIPID supervisory control. $\boldsymbol{L}^T$ is theoretical leg length vector. $\boldsymbol{L}^{\mathrm{R}}$ is the practical leg length vector, and $\boldsymbol{L}^{\mathrm{C}}$ is the leg length control value. ${}^{\mathrm{G}}\boldsymbol{X}_{\mathrm{PT}}$ is the practical position and orientation of the platform in the global frame. ${}^{\mathrm{G}}\boldsymbol{X}_{\mathrm{BR}}$ and ${}^{\mathrm{G}}\tilde{\boldsymbol{X}}_{\mathrm{BR}}$ are the practical and predicted position and orientation of the cabin in the global frame, respectively.

The digital PID filters loop algorithms – with acceleration and velocity feedforward – are used in the executive level of the linear actuators. The controller parameters listed in Table I are set when the motors are loaded.

## 6. Experimental Results

To validate the motion prediction algorithm and the supervisory control strategy discussed above, a series of experiments on the FAST 50 m model have been carried out. Figure 7 shows a photo of the filed model experiment. The

https://doi.org/10.1017/S0263574711000282 Published online by Cambridge University Press

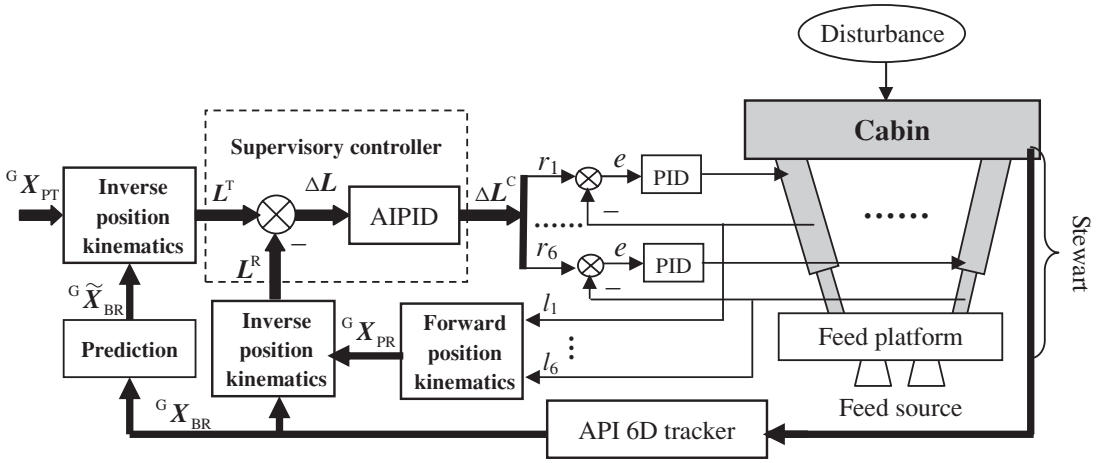


Fig. 6. AIPID supervisory control of the macro–micro parallel manipulator.

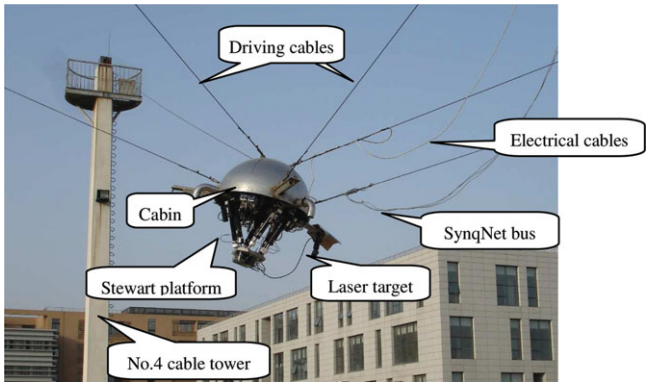


Fig. 7. Photo of the field model experiment.

position and orientation of the cabin were obtained with the API laser tracker. The position and orientation of the feed platform were calculated by the coordinate transformation and the forward position kinematics of the Stewart platform, according to the feedback values of the six legs.

The platform is desired to move along the astronomical observation trajectory, which can be given by the following equations. The desired linear velocity of the cabin and platform is 0.5 cm/s.

$$\begin{cases} x = 0.533 r_c (\sin\varphi \cos\sigma \cos H_t - \cos\varphi \sin\sigma), \\ y = 0.533 r_c \cos\sigma \sin H_t, \\ z = r_c - 0.533 r_c (\cos\varphi \cos\sigma \cos H_t + \sin\varphi \sin\sigma), \end{cases} \tag{23}$$

where $r_c = 35.35$ m is the radius of curvature of the main reflector, and $\varphi = 25^\circ$ is the geographical latitude of the observation point. $(\sigma, H_t)$ is the coordinate of the radio source in the astronomical coordinate system. $\sigma = 30^\circ$ is the declination of the radio source. $H_t$ is the hour angle of the radio source, and here, $-8^\circ \le H_t \le 8^\circ$. The wind speed of the filed model is approximately 1.2 m/s. The experimental results of the macro–micro parallel manipulator are as follows.

According to the astronomical observation specifications, the RMS of positioning error should be less than 4 mm, and the pointing error should be less than 0.0667°, when the FAST 50 m model is running. Figure 8 shows the theoretical and practical trajectories of the cabin and feed platform

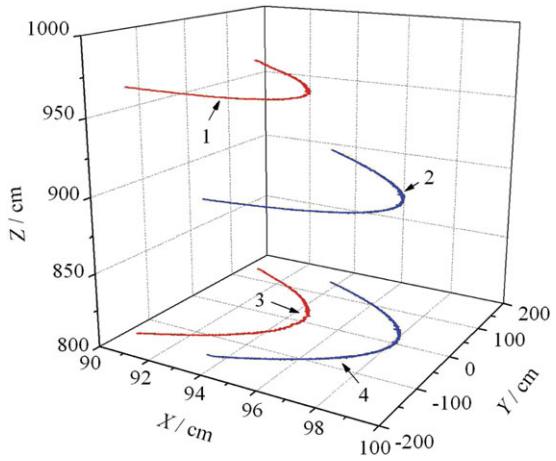


Fig. 8. 1. Trajectory of the cabin (macro). 2. Trajectory of the feed platform (micro). 3. Projection of curve 1. 4. Projection of curve 2. Trajectories and projections of the macro–micro parallel manipulator system.

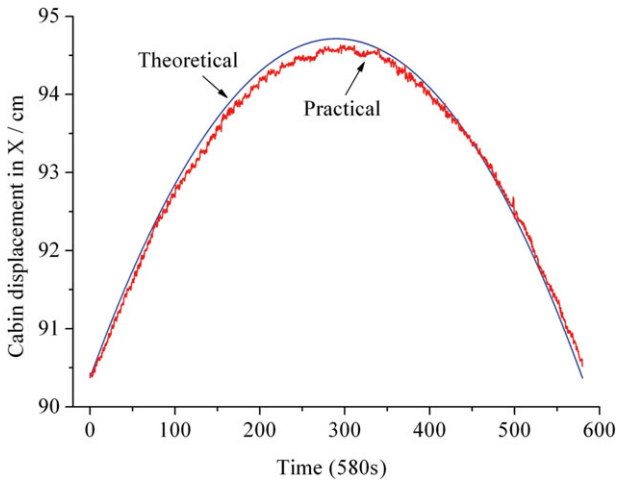


Fig. 9. Cabin displacement in $X$.

and their projection on the $XY$ plane. Figures 9, 10, and 11 show the theoretical and practical displacement of the cabin in the $X$-, $Y$-, and $Z$-directions, respectively. As for the $X$-displacement, between 100th and 450th s, the theoretical and practical curves depart from each other obviously. Except

https://doi.org/10.1017/S0263574711000282 Published online by Cambridge University Press

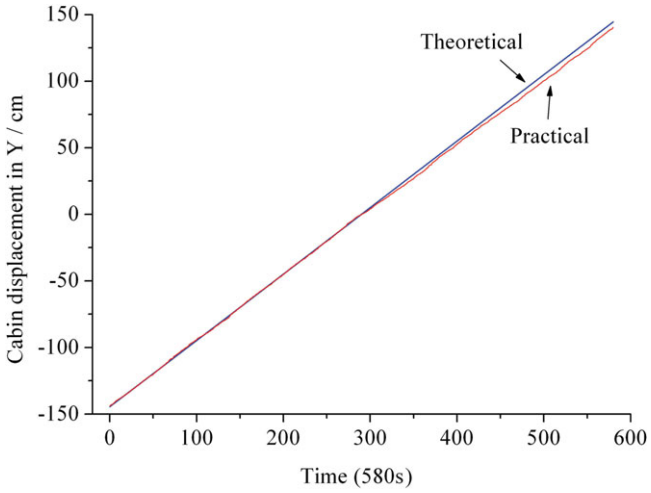


Fig. 10. Cabin displacement in *Y*.

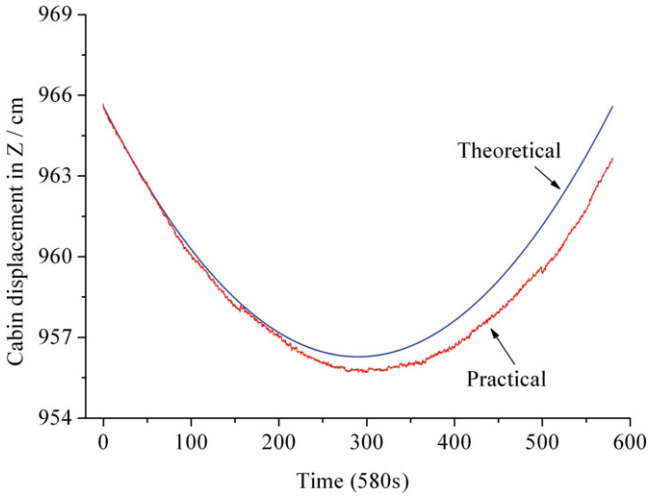


Fig. 11. Cabin displacement in *Z*.

during this time interval, the two curves almost coincide. In the *Y*-direction, the cabin and feed platform follow a uniform rectilinear motion, so the deviation between the theoretical and practical curves is quite small. After the 200th s, the position curves in the *Z*-direction depart from each other. This phenomenon can be explained straightforwardly because the macro parallel manipulator is driven by six flexible cables, and it has less positioning precision.

For comparison, Figs. 12, 13, and 14 show the positioning error of the cabin and platform in the *Z*-direction. It is shown that as a result of the flexibility of the six large span cables, the positioning error in the *Z*-direction of the cabin (macro manipulator) is over 2 cm, while the positioning error of the feed platform (macro manipulator) is limited to 2.5 mm. The micro parallel manipulator reduced the positioning error of the cabin in the *Z*-direction by 9/10. Furthermore, the distribution of the platform errors is quite stationary. The control effect satisfies the positioning specifications completely.

As mentioned in Section 2, the pitch angle precision of the platform will affect the observing result of the telescope, so it should be addressed first. Figure 15 shows the pitch angle error curves of the macro–micro parallel manipulator. The maximum pitch angle error of the cabin is up to 0.8°,

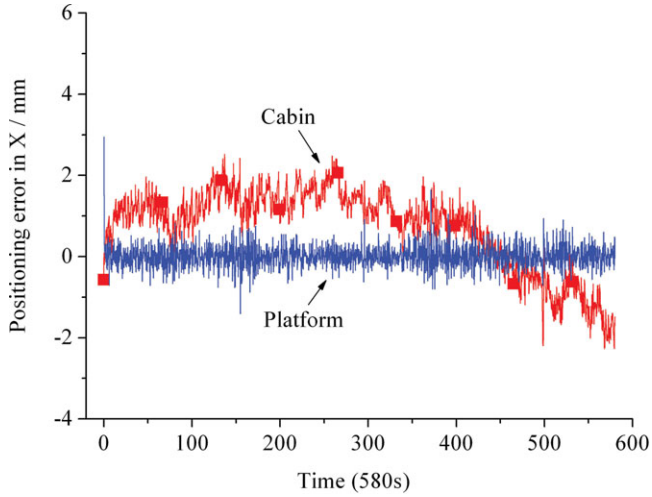


Fig. 12. Positioning error in *X* of the cabin and feed platform.

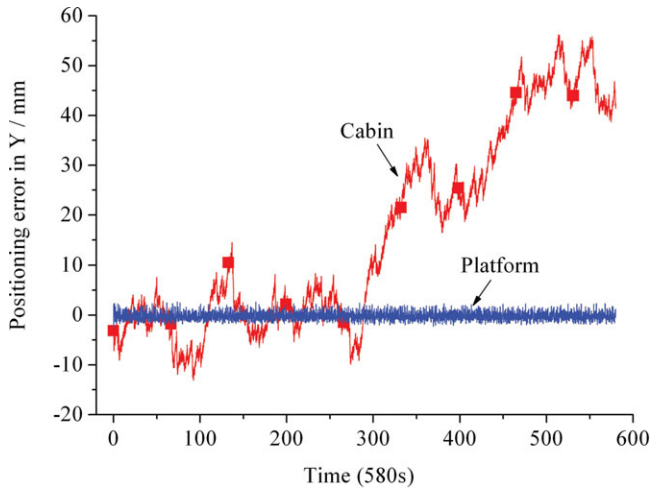


Fig. 13. Positioning error in *Y* of the cabin and feed platform.

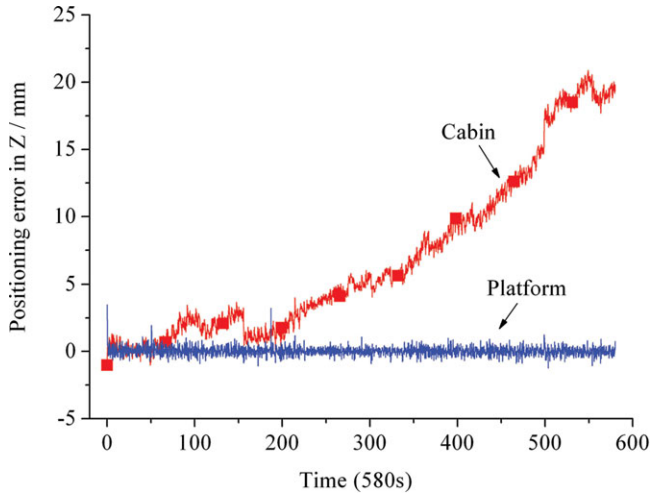


Fig. 14. Positioning error in *Z* of the cabin and feed platform.

while the pitch angle error of the platform is restricted to 0.06°. In addition, the pitch angle error of the platform is quite uniform.

In order to validate the supervisory controller of the macro–micro parallel manipulator system, astronomical trajectory

https://doi.org/10.1017/S0263574711000282 Published online by Cambridge University Press

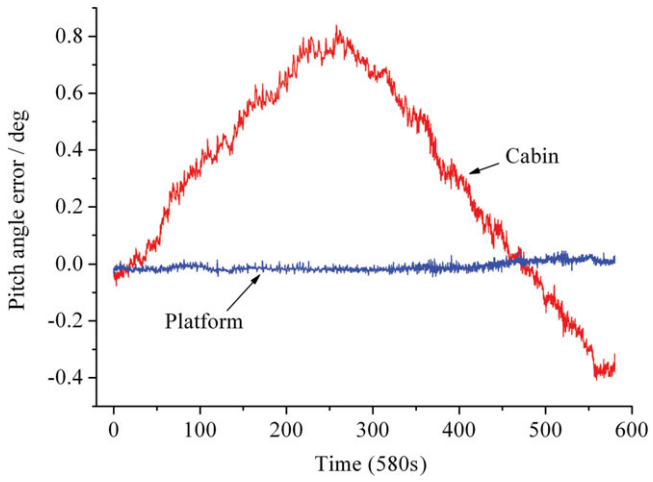


Fig. 15. Pitch angle error of the cabin and feed platform.

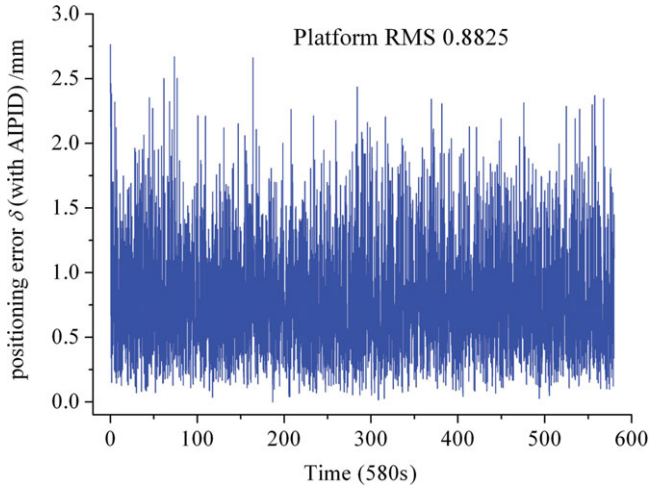


Fig. 16. Positioning error of the platform with supervisory control.

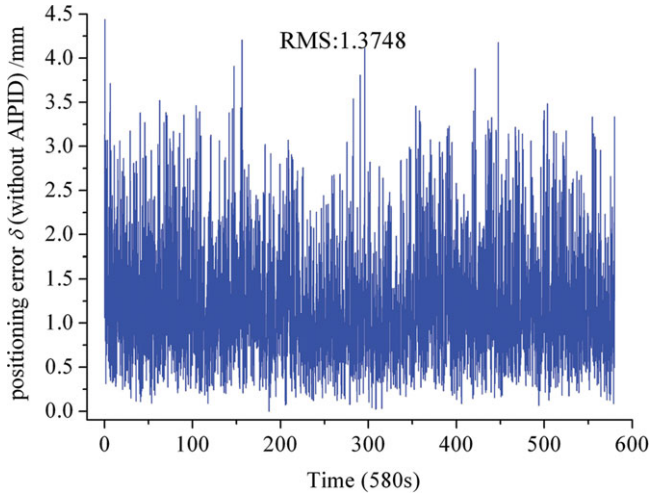


Fig. 17. Positioning error of the platform without supervisory control.

tracking experiments without an AIPID supervisory controller were conducted. Figures 16 and 17 show the curves of the $X$-, $Y$-, and $Z$-directions, with integrated positioning error $\delta = \sqrt{\delta X^2 + \delta Y^2 + \delta Z^2}$. This shows that the Stewart platform responses for the positioning and orientation error of the cabin dramatically without the planning control of the supervisory controller. The stronger reacting forces of the Stewart platform tend to induce the dynamical coupling phenomenon, so the positioning error of the platform is larger and up to 4.5 mm. The supervisory controller results in better performance compared with that case. By revising the planning control value substantially, the RMS of the positioning error of the platform is reduced by 35.7%.

## 7. Conclusions

The feed supporting, positioning, and tracking system for FAST is a macro–micro parallel manipulator. The measurement, control, and experiment of the macro–micro parallel manipulator have been investigated in this paper. The conclusions are drawn as follows:

(1) In order to overcome the shortcomings of the conventional prediction algorithm, a new tracking and prediction algorithm based on the theory of parallel mechanism is presented. By applying the nonlinear tracking differentiator and real-time steepest descent algorithm for forward position kinematics, this algorithm achieves the precise future position and orientation of the cabin.

(2) The simplified model of the linearized adaptive interaction algorithm is utilized to adjust the parameters of PID controllers, which constitute the AIPID controller. In order to overcome the control difficulty of the macro–micro parallel manipulator system, the AIPID controller is devised as the supervisory controller in the joint space of the micro parallel manipulator.

(3) The experimental results of the FAST50 m field model validate the effectiveness of the adaptive PID supervisory controller, accompanied by the motion predication of the cabin. The feed supporting, pointing, and tracking system could meet the demands of positioning and orientating precision with the desired tracking velocity.

## Acknowledgments

This work was supported by the Fundamental Research Funds for the Central Universities under Grant Nos. JY10000904011 and JY10000904013 and the National Natural Science Funds of China under Grant No. 50775170. The authors would like to appreciate the Editor, Associate Editor, and the reviewers for their valuable comments and suggestions.

## References

1. R. Nan, "Five hundred meter aperture spherical radio telescope (FAST)," *Sci. China, Ser. G: Phys. Astron.* **49**(2), 129–148 (2006).
2. P. A. Castleberg and K. M. Xilouris, "Arecibo observatory," *IEEE Potentials* **16**(3), 33–35 (1997).
3. A. W. Love, "Arecibo observatory 40th anniversary celebration," *IEEE Potentials* **23**(2), 41–44 (2004).
4. B. Y. Duan, "A new design project of the line feed structure for large radio telescope and its nonlinear dynamic analysis," *Mechatronics* **9**(1), 53–64 (1999).
5. B. Zi, B. Y. Duan, J. L. Du and H. Bao, "Dynamic modeling and active control of a cable-suspended parallel robot," *Mechatronics* **18**(1), 1–12 (2008).

https://doi.org/10.1017/S0263574711000282 Published online by Cambridge University Press

6. L. E. George, Active Vibration Control of a Flexible Base Manipulator *PhD Dissertation* (Atlanta, GA: Georgia Institute of Technology, 2002).
7. J. Lin and Z. Z. Huang, "A novel PID control parameters tuning approach for robot manipulators mounted on oscillatory bases," *Robotica* **25**(4), 467–477 (2007).
8. J. Y. Lew and S. M. Moon, "A simple active damping control for compliant base manipulators," *IEEE/ASME Trans. Mechatronics* **6**(3), 305–310 (2001).
9. O. Begovich, E. N. Sanchez and M. Maldonado, "Takagi-Sugeno fuzzy scheme for real-time trajectory tracking of an underactuated robot," *IEEE Trans. Control Syst. Technol.* **10**(1), 14–20 (2002).
10. B. Dasgupta and T. S. Mruthyunjaya, "A Newton-Euler formulation for the inverse dynamics of the Stewart platform manipulator," *Mech. Mach. Theory* **33**(8), 1135–1152 (1998).
11. S. Fu, Y. Yao and Y. Wu et al., "Comments on "A Newton-Euler formulation for the inverse dynamics of the Stewart platform manipulator by B. Dasgupta and T. S. Mruthyunjaya [*Mech. Mach. Theory* **33**, 1135–1152 (1998)]," *Mech. Mach. Theory* **42**(12), 1668–1671 (2007).
12. A. Sharon, N. Hogan and D. E. Hardt, "The macro/micro manipulator: An improved architecture for robot control," *Robot. Comput–Integr. Manuf.* **10**(3), 209–222 (1993).
13. D. P. Magee and W. J. Book, "Filtering Micro-Manipulator Wrist Commands to Prevent Flexible Base Motion," *Proceedings of Proceedings of the 1995 American Control Conference. Part 1 (of 6)*, Seattle, WA, USA (Jun. 21–23, 1995) pp. 924–928.
14. J. Y. Lew and D. J. Trudnowski, "Vibration control of a micro/macro-manipulator system," *IEEE Control Syst. Mag.* **16**(1), 26–31 (1996).
15. W. Yim and N. S. Sahjendra. "Nonlinear Inverse and Predictive End Point Trajectory Control of Flexible Macro-Micro Manipulators," *Proceedings of the 13th World Congress of IFAC. Vol. A: Robotics, Components and Instruments*, San Francisco (1996) pp. 97–102.
16. I. Sharf, "Active Damping of a Large Flexible Manipulator with a Short-Reach Robot," *Proceedings of the 1995 American Control Conference. Part 1 (of 6),* Seattle, WA, USA (Jun. 21–23, 1995) pp. 3329–3333.
17. X. P. Cheng and R. V. Patel, "Neural network based tracking control of a flexible macro-micro manipulator system," *Neural Netw.* **16** (2), 271–286 (2003).
18. H. Bassan, H. A. Talebi, R. V. Patel and M. Moallem "Control of a rigid manipulator mounted on a compliant base," *Robotica* **23** (2), 197–206 (2005).
19. A. Mannani and H. A. Talebi, "A fuzzy Lyapunov-based control strategy for a macro-micro manipulator: Experimental results," *IEEE Trans. Control Syst. Technol.* **15** (2), 375–383 (2007).
20. B. Y. Duan, Y. Y. Qiu and F. S. Zhang et al., "On design and experiment of the feed cable-suspended structure for super antenna," *Mechatronics* **19**(4), 503–509 (2009).
21. T. Li, H. Zheng, J. Wang and G. Duan, "Precision measures for various configuration of parallel kinematic machine tools," *Chinese J. Mech. Eng.* **38**(9), 101–105 (2002).
22. X. C. Duan, Y. Y. Qiu and B. Y. Duan, "Analysis of servo bandwidth of the fine tuning Stewart platform for the large radio telescope," *Zhongguo Jixie Gongcheng/China Mech. Engng* **16**(3), 245–248 (2005).
23. J. Han, *Active Disturbance Rejection Control Technique-The Technique for Estimating and Compensating the Uncertainties* (National Defense Industry Press, Beijing, 2008).
24. J. Han, "Active disturbances rejection control technique," *Frontier Sci.* **1**(1), 24–31 (2007).
25. Y. Wang, "A direct numerical solution to forward kinematics of general Stewart-Gough platforms," *Robotica* **25**(1), 121–128 (2007).
26. Y. Yuan and W. Sun, *Optimized Theory and Methods* (Science Press, Beijing, 2003).
27. R. D. Brandt and F. Lin, "Supervised learning in neural networks without feedback network," *Proceedings of the 1996 IEEE International Symposium on Intelligent Control*, Dearborn, MI, USA (Sep. 15–18, 1996) pp. 86–90.
28. F. Lin, R. D. Brandt and G. Saikalis, "Self-tuning of PID controllers by adaptive interaction," *Proceedings of American Control Conference*, Chicago, IL, USA (Jun. 28–30, 2000) pp. 3676–3680.


https://doi.org/10.1017/S0263574711000282 Published online by Cambridge University Press